Coherent magnetotransport in confined arrays of antidots. I. Dispersion relations and current densities

I. V. Zozoulenko,* Frank A. Maaø, and E. H. Hauge
Institutt for fysikk, Universitetet i Trondheim, Norges Tekniske Høgskole, N-7034, Trondheim, Norway
(Received 26 June 1995)

The energy band structure of an antidot array defined in a strip geometry of finite width is calculated as a function of the magnetic field, in a parameter range typical of existing experiments, and with edge aspects explicitly taken into account. The calculations are based on a hybrid recursive Green-function technique specially adapted to problems of this type. The current densities associated with representative Bloch states are calculated and visualized. At a given Fermi energy and in zero magnetic field, the set of propagating Bloch states consists of fast states with essentially one-dimensional laminar type flow, channeling between rows of antidots, and slower ones with a genuinely two-dimensional flow of vortex character. Simple physical arguments are used to explain the existence of the different types of states. At low magnetic fields much of the character of the zero-field states is retained. At magnetic fields sufficiently high that the classical cyclotron diameter is close to the lattice constant of the array, the magnetobands correspond to edge states and to states of the ''runaway'' type, in which electrons bounce off antidots in consecutive unit cells. Surprisingly, states corresponding to electrons in classical orbits pinned around single antidots play only a minor role. With a further increase of the magnetic field, essentially only edge states survive. In this high-field regime, states beyond the edge states only exist in narrow energy bands, and these states correspond to bulk transport with electrons hopping between quasilocalized states.

I. INTRODUCTION

During the past few years the study of electron magnetotransport in lateral antidot superlattices has been a topic of considerable interest, both from an experimental[1–14] and a theoretical[15–22] point of view. Such superlattices are fabricated by defining in the two-dimensional electron gas (2DEG) periodic arrays of islands with strong repulsive potential, called antidots. The initial motivation for studying magnetotransport in such structures was the opportunity to access the regime of the Hofstadter ''butterfly'' energy spectrum.[23] As the typical size of the lattice constant of antidot lattices ranges from 150 nm to 1 μm, the characteristic effects of this spectrum are expected to be found in the easily accessible field range below 1 T. Whatever the motivation, the experimental studies of magnetotransport in antidot arrays revealed a rich variety of sometimes unexpected effects. In particular, a series of peaks in the diagonal magnetoresistivity ρ_{xx} were found. These are believed to occur when commensurability conditions are fulfilled between the superlattice period and the classical cyclotron radius $r_c=\hbar k_F/eB$ at the Fermi momentum $\hbar k_F$.

Most of the theoretical work on magnetotransport in antidot lattices has been based on classical mechanics. The classical explanation of the magnetoresistance maxima is that electrons pinned in orbits around (or between) groups of antidots are removed from the transport process and, therefore, do not contribute to the conductivity. This leads to an increase in ρ_{xx}. The picture was somewhat modified by Fleischmann, Geisel, and Ketzmerick[15] who showed that regular pinned orbits play only a minor role in determining the conductivity. Instead, chaotic (quasipinned) orbits, trapped around or between groups of antidots for a long time, cause the peaks in the magnetoresistance. As the theoretical calculations fit the experimental data, the above picture was widely accepted as correct.

However, Baskin *et al.*[16] have pointed to a different mechanism. They found, again on the basis of classical mechanics, that stable ''runaway'' trajectories rolling along different rows of the antidot lattice are responsible for an enhancement of the diagonal *conductivity* σ_{xx}. Runaway trajectories were recently used by Schuster *et al.*[12] in the interpretation of their experiments. They found that the off-diagonal terms of the resistivity tensor play an important role and that pronounced maxima in the magnetoresistance correspond not to minima in the conductance as one could expect, but to *maxima*, consistent with the existence of runaway trajectories.

Quantum-mechanical calculations of the magnetoconductance of antidot lattices have been performed in Refs. 18,19,21,22. These calculations start from different versions of the Kubo formula. The agreement between the theoretical predictions of Ref. 21 and experimental data[5] is almost quantitative. However, in contrast to the classical theories quoted above, it is difficult to relate these conductivity results to particular types of electron dynamics.

So far, most experimental and theoretical work has concentrated on essentially *macroscopic* structures. In such systems the phase coherence length l_ϕ as well the elastic mean free path l_e are much smaller than the size of the sample. Thus, phase-breaking events destroy coherence, and bulk magnetotransport can be described in the framework of Drude-type models.[24] Recently, magnetotransport in *mesoscopic* lattices with total dimensions smaller than both l_ϕ and l_e has been studied.[11] Again, like in macroscopic samples, an oscillatory structure was found in the magnetoresistance.

However, phase coherence effects manifested themselves in reproducible quantum fluctuations superimposed onto the commensurate peaks.

With coherent transport through mesoscopic systems, the Landauer-Büttiker[25,26] formalism is the appropriate one for the computation of linear transport coefficients. In a magnetic field, the incoming propagating modes are edge states[27] localized at one of the edges of the sample. In the absence of scatterers, the two-terminal as well as the Hall conductance of the sample are simply proportional to the number of propagating edge states. This highlights the fact that with coherent transport in confined geometries, with or without antidots, edge states should always be taken explicitly into account. In an earlier publication[28] we studied magnetotransport through a confined array of antidots in the extreme quantum limit, when the lattice constant of the antidot array is of the order of the Fermi wavelength. The dependence of the conductance on the Fermi energy and on the magnetic field was analyzed on the basis of the band structure of the corresponding infinite superlattice. This approach turned out to be very successful for the interpretation of the two-terminal conductance $\mathscr{G}_{2t}$ of *finite* antidot arrays, since the features of $\mathscr{G}_{2t}$ could be directly attributed to contributions from corrsponding minibands. Each of these minibands was associated with a particular type of electron motion. In this way, complex behavior of the conductance could be given a direct physical interpretation. Thus, the main virtue of the classical simulations, that of providing the physical mechanisms underlying the conductance results, could be taken into the quantum regime and, moreover, studied in the confined geometry used in a typical experiment.

However, the results of Ref. 28 were limited to the extreme quantum regime of small electron density and one or two Landau levels in the leads. In contrast, existing experiments on mesoscopic arrays of antidots in confined geometries are performed in the semiclassical regime, where the Fermi wavelength λ_F is (much) smaller than the period of the superlattice. With the introduction of a hybrid between two numerical techniques commonly used in this field, we have been able to access the semiclassical regime. Thus, the purpose of the present paper and its sequel[29] (hereafter referred to as paper II) is to extend our previous calculations to the region of principal experimental interest. In this paper we study the magnetic band structure and current densities of the corresponding Bloch states. In Sec. II we develop the hybrid Green-function technique for the calculation of the magnetoband structure. That section will also serve as the theoretical basis for paper II in this series. In Sec. III the band structure, as it evolves with increasing magnetic field, is discussed. Particular emphasis is given to the current density associated with the different states. Section IV contains a brief summary of the results obtained so far. On the basis of the results of this paper, the two-terminal conductance of various lengths of antidot lattices in a strip geometry will be discussed in paper II.

II. THEORY

In this section we present the Green-function formalism basic to our calculations. Under study are two-dimensional (2D) systems confined in the transverse (n) direction, periodic in the longitudinal (m) direction with period L, and placed in a perpendicular magnetic field $\mathbf{B}=\hat{z}B$. It is convenient to split the potential energy into two parts, $v_{mn}^{\rm conf}$ and v_{mn}, where $v_{mn}^{\rm conf}$ is the confining potential, and v_{mn} will be used to describe the antidots. Lengths, like L, will be measured in units of the lattice constant a of the underlying tight-binding lattice, see Fig. 1. Choosing the Landau gauge $\mathbf{A}=(-Ban,0,0)$ and following Peierls in incorporating the magnetic field by a phase factor in the hopping amplitudes, we arrive at the Schrödinger equation $H\Psi=E\Psi$, where the matrix element $\langle m,n|\Psi\rangle=\psi_{mn}$ defines the probability amplitude to find the electron on site (m,n). The corresponding tight-binding Hamiltonian reads

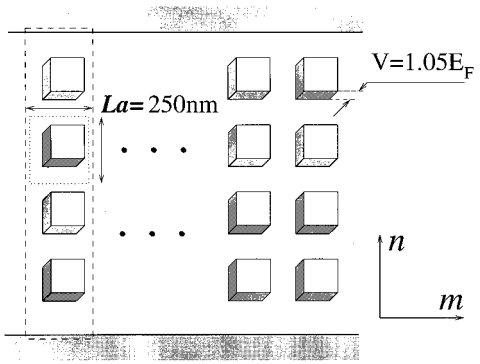

FIG. 1. Schematic geometry of the periodical antidot lattice. The dashed-line rectangle indicates the one-dimensional elementary unit cell.

$$H=\sum_{m,n}\left(|m,n\rangle(\epsilon_0+v_{mn}^{\rm conf}+v_{mn})\langle m,n|-t\{|m,n\rangle\langle m,n+1| + |m,n\rangle e^{-iqn}\langle m+1,n|+\text{H.c.}\}\right). \quad (1)$$

Here t is the nearest-neighbor hopping amplitude at zero magnetic field, ϵ_0 is the lattice site electron energy, and $q=eBa^2/\hbar$. In our calculations we set $\epsilon_0=4t$. Together with the choice $t=\hbar^2/2m^*a^2$, with m^* the effective mass, this ensures that, in the continuum limit $[ma\to x,na\to y,a\to 0;\psi_{mn}\to\psi(x,y)]$, the above tight-binding approach yields the familiar Schrödinger equation in the effective-mass approximation

$$\frac{\hbar^2}{2m^*}\left[\left(\frac{\partial}{\partial x}-\frac{ieBy}{\hbar}\right)^2+\frac{\partial^2}{\partial y^2}\right]\psi(x,y) = [v^{\rm conf}(x,y)+v(x,y)-E]\psi(x,y). \quad (2)$$

Note that with the gauge chosen, the magnetic unit cell (in the x direction) coincides with the superlattice period $La\to\mathscr{L}$. We require, furthermore, that the confining potential respects the discrete translational invariance of the superlattice. Thus, the Bloch theorem dictates that solutions of the Schrödinger equation are of the form[30]

$$\psi(x,y)=e^{ikx}u_k(x,y);u_k(x+\mathscr{L},y)=u_k(x,y). \quad (3)$$

A standard numerical method to study such problems is the transfer matrix technique.[31] In that approach one expands, for a given x, the transverse wave function in the

eigenfunctions of the transverse motion (the transverse modes). After discretizing the geometry in the longitudinal direction and matching the wave functions and their derivatives on the boundaries of the segments, one arrives at a system of coupled equations for the determination of the transfer matrix, the rank of which is determined by the number, N_{modes}, of transverse modes taken into account. Diagonalization gives eigenvalues k_α and eigenfunctions ψ_α of (2). However, this technique, at least in its simplest versions, is plagued by numerical instability problems caused by components growing exponentially during the iteration process (see, for example, Ref. 32).

An alternative, generally used in connection with tight-binding models, is the recursive Green-function technique.[26,33,34] It has the important virtue of numerical stability, in addition to being quite flexible. Its weakness is associated with the fact that the geometry must be discretized in both transverse and longitudinal directions. This makes it difficult to model wide or smoothly varying structures, since the transverse number of sites N_{sites} associated with the widest part of the geometry determines the rank of matrices to be inverted a large number of times. Generally, $N_{\text{sites}} \gg N_{\text{modes}}$, making the recursive Green-function technique extremely time consuming for complex geometries.

In our calculations we use a hybrid technique that takes advantage of the strengths of both methods, while avoiding their weaknesses. This technique has been introduced earlier[35] for the case of zero magnetic field. In this paper we shall demonstrate its utility in the presence of a magnetic field. In our hybrid approach, we use the local transverse (field free) energy modes as a basis. This allows great flexibility in modeling smooth geometries within a function space of reasonable dimensionality. On the other hand the recursive Green-function technique is used in the (discretized) longitudinal direction to determine the transfer matrix. This eliminates numerical instability problems from the calculation of the transfer matrix.

Rewrite the Schrödinger equation with Hamiltonian (1) in the hybrid space-energy representation, passing from the discrete transverse coordinate n to the continuous one y, $\psi_{mn} \rightarrow \psi_m(y)$. At this point we introduce dimensionless quantities. Lengths will be measured in units of the basic length a, wave numbers in units of a^{-1}, and energies in units of $t = \hbar^2/2m^* a^2$ (implying that $t=1$). In these dimensionless units, expand the wave function in the set of (real) eigenfunctions $\{f_j^m(y)\}$ generated by the (local in m) continuous Schrödinger equation

$$\left[-\frac{\partial^2}{\partial y^2} + v_m^{\text{conf}}(y) \right] f_j^m(y) = \varepsilon_j^m f_j^m(y), \tag{4}$$

with ε_j^m the corresponding eigenvalue.

In this basis the matrix element

$$\langle m,j|\Psi\rangle = \int dy\ f_j^m(y)\psi_m(y) \tag{5}$$

defines the probability amplitude to find an electron on slice m in energy state j. The Hamiltonian (1) in hybrid representation reads

$$H = \sum_m \left[\sum_i^N |m,i\rangle(\varepsilon_i^m + 2)\langle m,i| + \sum_{ij}^N |m,i\rangle v_{ij}^m \langle m,j| - \sum_{ij}^N \left(|m,i\rangle V_{ij}^{m,m+1}\langle m+1,j| + |m+1,i\rangle U_{ij}^{m+1,m}\langle m,j| \right) \right], \tag{6}$$

where

$$U_{i,j}^{m+1,m} = \int dy\ e^{iqy} f_i^{m+1}(y) f_j^m(y), \tag{7a}$$

$$V_{i,j}^{m,m+1} = (U_{j,i}^{m+1,m})^*, \tag{7b}$$

$$v_{i,j}^m = \int dy\ f_i^m(y) f_j^m(y) v_m(y). \tag{7c}$$

The set of transverse modes $\{f_j^m(y)\}$ is restricted to the N lowest ones, where N is determined from the numerical accuracy required. The Hamiltonian (6) has only nearest-neighbor couplings in the longitudinal m direction. In the transverse (''energy'') direction, the magnetic field couples all states i on slice m to all states j on neighboring slices $m-1$ and $m+1$. The strength of the coupling is defined by the matrix elements $U_{ij}^{m+1,m}, V_{ij}^{m,m+1}$ [Eqs. (7a) and (7b)]. The presence of the potential $v_m(y)$ causes mixing of the states on a single slice m, with matrix elements v_{ij}^m [Eq. (7c)].

Consider one unit cell of the superlattice with the first slice $m=1$ and the last one $m=L$. Write down the total Hamiltonian (6) in the form

$$H = \mathscr{H}_{\text{cell}} + \mathscr{H}_{\text{out}} + \mathscr{V}. \tag{8}$$

Here $\mathscr{H}_{\text{cell}}$ represents the unit cell under consideration, and $\mathscr{H}_{\text{out}}$ the remainder of the superlattice, with the term $\mathscr{V}$ containing all the couplings between the two,

$$\mathscr{V} = -\sum_{ij} \left(|0,i\rangle V_{ij}^{0,1}\langle 1,j| + |1,i\rangle U_{ij}^{1,0}\langle 0,j| + |L,i\rangle V_{ij}^{L,L+1}\langle L+1,j| + |L+1,i\rangle U_{ij}^{L+1,L}\langle L,j| \right). \tag{9}$$

Introduce the Green function $G = (E - \mathscr{H}_{\text{cell}})^{-1}$. We can then write down the formal solution of the Schrödinger equation as

$$|\psi_{\text{cell}}\rangle = G\mathscr{V}|\psi_{\text{out}}\rangle, \tag{10}$$

with $|\psi_{\text{cell}}\rangle$ the wave function in the cell under consideration, and $|\psi_{\text{out}}\rangle$ that outside.

Let us introduce the notation $\vec{\psi}_m$ for the column vector composed of matrix elements $\langle m,j|\Psi\rangle; 1 \leq j \leq N$. Using Eqs. (10) and (9) one can express the states $\vec{\psi}_1$ and $\vec{\psi}_L$ on the boundaries of the cell by those on slices adjacent to the cell,

$$-\vec{\psi}_1 = \mathbf{G}^{11}\mathbf{U}^{1,0}\vec{\psi}_0 + \mathbf{G}^{1L}\mathbf{V}^{L,L+1}\vec{\psi}_{L+1}, \tag{11}$$

$$-\vec{\psi}_L = \mathbf{G}^{L1}\mathbf{U}^{1,0}\vec{\psi}_0 + \mathbf{G}^{LL}\mathbf{V}^{L,L+1}\vec{\psi}_{L+1}.$$

Here $\mathbf{G}^{L,L'}$ is a shorthand notation for the matrix $\langle L,i|\mathbf{G}|L',j\rangle$, with similar definitons of $\mathbf{U}^{m,m'}$ and $\mathbf{V}^{m,m'}$. The actual calculation of the $N\times N$ matrices $\mathbf{G}^{m,m'}$ starts, in standard fashion,[26,34] from the matrix on the isolated slice No. 1, and adds slices up to No. L by systematic use of the Dyson equation. Equation (11) can be rewritten in terms of the transfer matrix $\mathbf{T}$ relating the wave functions on the slices $m=L+1,L$ to those on $m=1,0$,

$$\begin{pmatrix} \vec{\psi}_{L+1} \\ \vec{\psi}_L \end{pmatrix} = \mathbf{T} \begin{pmatrix} \vec{\psi}_1 \\ \vec{\psi}_0 \end{pmatrix}, \tag{12}$$

where

$$\mathbf{T} = \begin{pmatrix} -\mathbf{G}^{1L}\mathbf{V}^{L,L+1} & 0 \\ \mathbf{G}^{LL}\mathbf{V}^{L,L+1} & \mathbb{1} \end{pmatrix}^{-1} \begin{pmatrix} \mathbb{1} & \mathbf{G}^{11}\mathbf{U}^{1,0} \\ 0 & -\mathbf{G}^{L1}\mathbf{U}^{1,0} \end{pmatrix},$$

with $\mathbb{1}$ the unit matrix. Using the hybrid basis we can rewrite the Bloch theorem (3) in the form

$$\vec{\psi}_{L+m} = e^{iKL}\vec{\psi}_m . \tag{13}$$

Combining (12) and (13) we arrive at the $2N\times 2N$ set of equations

$$\mathbf{T} \begin{pmatrix} \vec{\psi}_1 \\ \vec{\psi}_0 \end{pmatrix} = \begin{pmatrix} \mathbb{1}e^{iKL} & 0 \\ 0 & \mathbb{1}e^{iKL} \end{pmatrix} \begin{pmatrix} \vec{\psi}_1 \\ \vec{\psi}_0 \end{pmatrix}, \tag{14}$$

which have $2N$ eigenvalues $K_\alpha^{\pm}$, $1\leqslant\alpha\leqslant N$; K_α^{+} with corresponding eigenfunctions $\psi_{1\alpha}^{+},\psi_{0\alpha}^{+}$ represent states propagating $[\partial E/\partial K>0$, $\mathrm{Im}(K)=0]$ or decaying $[\mathrm{Im}(K)>0]$ to the right, whereas K_α^{-} with corresponding eigenfunctions $\psi_{1\alpha}^{-},\psi_{0\alpha}^{-}$ represent states propagating $[\partial E/\partial K<0$, $\mathrm{Im}(K)=0]$ or decaying $[\mathrm{Im}(K)<0]$ to the left. We shall only consider structures that are symmetric around the line $y=0$. In that case, $K_\alpha^{+}=-K_\alpha^{-}$. In the general case, $K_\alpha^{+}(B)=-K_\alpha^{-}(-B)$.

Having calculated the eigenvalues and eigenfunctions of the problem (14), and knowing all the matrices $\mathbf{G}$, one is able to calculate the spatial distribution of the particle current associated with the different Bloch states. Fundamentally, the current in tight-binding models is associated with hopping along *bonds*.[38] Nevertheless, for visualization purposes it is more convenient to view the local particle current density $\boldsymbol{j}_{mn}$ as a vector associated with *sites*. The corresponding expression is derived in standard fashion from a combination of the time-dependent Schrödinger and the continuity equation. It reads, in units of $t/a\hbar$,

$$\begin{aligned} \boldsymbol{j}_{mn}^{+\alpha} = -(i/2)\{ & \hat{\mathbf{m}}\psi_{mn}^{\alpha *}[e^{iqn}\psi_{m+1,n}^{\alpha} - e^{-iqn}\psi_{m-1,n}^{\alpha}] \\ & + \hat{\mathbf{n}}\psi_{mn}^{\alpha *}[\psi_{m,n+1}^{\alpha} - \psi_{m,n-1}^{\alpha}] - \text{c.c.}\}, \end{aligned} \tag{15}$$

where ψ_{mn}^{α} is the wave function (in real space representation) associated with the eigenvalue K_α, and $\hat{\mathbf{m}},\hat{\mathbf{n}}$ are the unit vectors in the longitudinal and transverse directions. Starting from our hybrid basis we, in practice, construct $\psi_m^{\alpha}(y)$ for use in (15), rather than ψ_{mn}^{α}. In the continuous limit Eq. (15) reduces to the standard definition of the current density in a magnetic field.[36]

To conclude this section, let us briefly summarize the virtues of the hybrid technique presented here. By using transverse eigenfunctions as a basis we were able to confine our function space to the minimum dimension necessary for the problem at hand. In this way the computational effort is considerably reduced in comparison with the original tight-binding formulation. The Green-function approach adopted in this section is numerically stable. In contrast, the standard version of the transfer matrix technique (which uses the same basis of transverse eigenstates) suffers from numerical stability problems sufficiently serious to make calculations for large-size structures with a strong modulation potential almost impossible.

Note that an alternative way of finding the Bloch solutions in the case of 2D periodic potential is based on the utilization of the finite-elements method.[37] This method, although numerically stable, requires essentially large-scale computations on supercomputers, especially at high magnetic fields. The present method, based on recursive Green-function techniques, requires only moderate computation facilities.

III. RESULTS AND DISCUSSION

A. System studied

In this section we examine the band structure and the nature of various Bloch states in antidot arrays, using the Green-function formalism developed in the previous section. The antidot array is confined to a strip with hard walls and of constant width w, and is infinite in the longitudinal direction. Already strips with four antidots across reveal the essential physics in this context. We shall, consequently, restrict ourselves to systems in which the one-dimensional unit cell of the corresponding (super) lattice consists of four antidots; see Fig. 1.

In the literature the antidot potential has been modeled by a δ-function potential,[18] circular hard disks,[16,17,19] a square potential,[28,31,32] or a soft cosine-type potential.[15,20–22] Presumably, the latter most adequately represents the experimental situation, in which the potential landscape is defined by gates sufficiently removed from the 2DEG to justify neglect of higher Fourier components. In our calculations we opt for the following pragmatic compromise: We model the antidots by a square potential with height just above the Fermi energy, $V=1.05E_F$. Because of the finite tunneling probability this potential corresponds to ''soft'' antidots with rounded corners. This is reflected in the current density patterns. As a consequence, in the figures showing the current distribution in various states, we shall draw the antidots as *rounded*, in spite of the fact that, geometrically, they are square. From a computational point of view the use of square antidots greatly facilitates our recursive Green-function technique. These calculations start from the first slice $m=1$ and add more slices by systematic use of the Dyson equation. In the general case of a varying potential, the iteration has to proceed one slice at a time. If, however, the potential landscape is the same for each step in the antidot region, one can calculate the Green function only for the first slice, and then effectively ''exponentiate'' the process by successively using

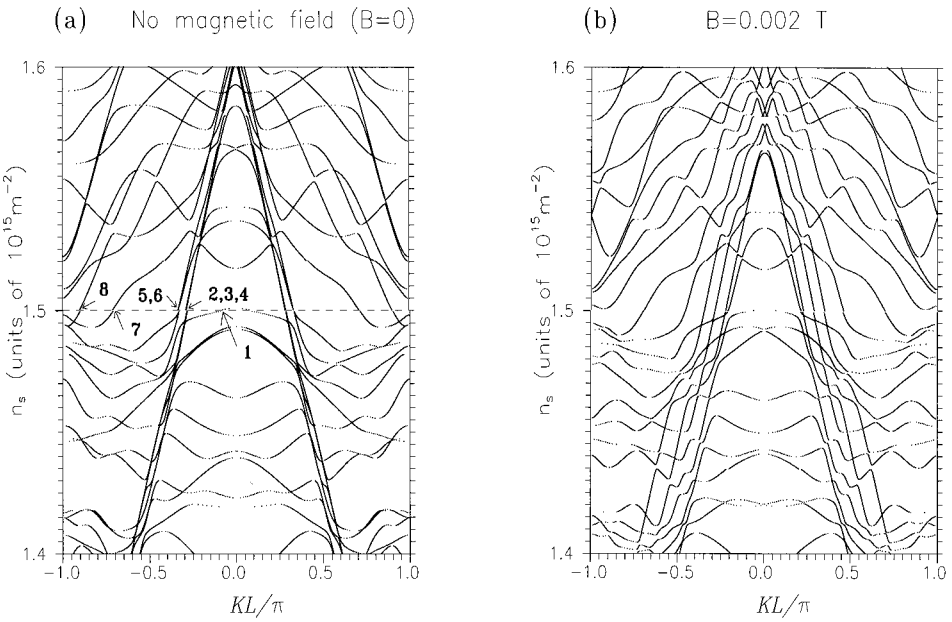

FIG. 2. (a) Band structure of the antidot lattice in zero magnetic field. (b) The effect of lifting the degeneracy of fast quasi-free-electron states in a weak magnetic field ($B=0.005$ T).

segments of 2,4, . . . ,2^p slices as basic elements in the iteration scheme.[38] This trick greatly reduces the computation time.

We choose the lattice constant of the antidot array as $La=250$ nm, with the antidot size equal to the distance between antidots. These parameter values are close to those used in the experiments of Schuster *et al.*[11] In our calculations we divide one unit cell into 64 slices. This corresponds to a lattice constant $a\approx 4$ nm of the underlying tight-binding lattice. With such a fine mesh, the tight-binding Hamiltonian (1) gives a description essentially equivalent to that of the continuum Schrödinger equation in the effective-mass approximation. It is the sheet electron density, $n_s=E_F m^*/\pi\hbar^2$ (with $m^*=0.067m_e$ for GaAs-$Ga_xAl_{1-x}As$ structures), rather than the Fermi energi E_F, which characterizes the samples and is controlled in experiments on the 2DEG. For this reason, rather than presenting the dispersion curves in the customary form $E=E(K)$, we prefer the rescaled equivalent $n_s=n_s(K)$ or its inverse $K=K(n_s)$.

B. Zero magnetic field

Figure 2(a) shows the calculated band structure of the antidot lattice in zero magnetic field, in the reduced zone representation ($-1<KL/\pi<1$). The band structure consists of a number of minibands. Between the various dispersion relations, both crossings and anticrossings (with minigaps) can be observed. In this complicated structure, we can qualitatively distinguish, at a given Fermi energy, dispersive (fast) quasi free-electron states, less dispersive (slower) ones, and almost dispersionless states. Due to the symmetry of the structure, every state propagating to the right has a mirror image propagating to the left. From here on we consider only states propagating to the right.

In order to understand the physical nature of the various Bloch states in the antidot superlattice, it is instructive to study the corresponding particle current density. In the typical experimental range, let us choose the electron sheet density as $n_s=1.5\times 10^{15}$ m^{-2} and examine all available Bloch states. At this value of n_s Fig. 2(a) shows that there are five fast quasi-free-electron states (marked by arrows 2 through 6), two slower ones (marked by arrows 7 and 8), and one almost dispersionless state (arrow 1). States 2–4 and 5–6 are almost degenerate and their dispersion curves are indistinguishable on the scale of the figure. Plots of the current density reveal the nature of these states; see Figs. 3 and 4. The threefold degenerate states 2–4 correspond to ballistic trajectories concentrated in the horizontal channels between two neighboring rows of antidots. We shall denote states of this kind ''channeling'' states. One example is shown in Fig. 3. In the antidot lattice under consideration there are only three equivalent paths of this type. This explains the threefold degeneracy. (For example, with finite w, *almost* degeneracy. Note that in zero magnetic field, every Bloch state has a current distribution symmetric around the central symmetry

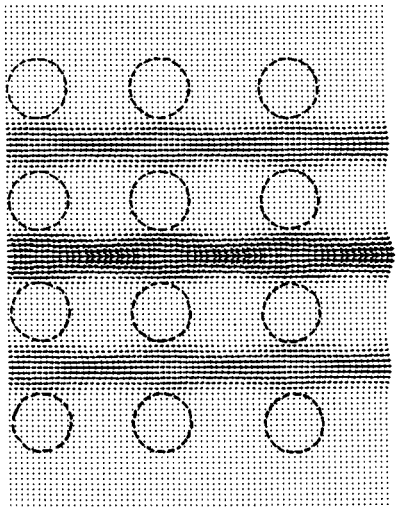

FIG. 3. The current density associated with state 2 in Fig. 2(a). In this and the other figures showing current densities associated with various Bloch states, the antidots are shown with their *effective* shape, as rounded, rather than as purely geometric squares.

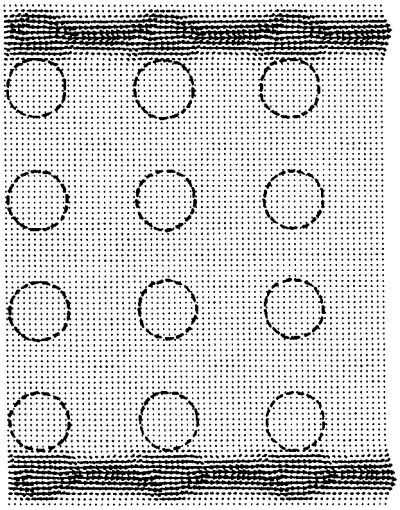

FIG. 4. The current density associated with state 5 in Fig. 2(a).

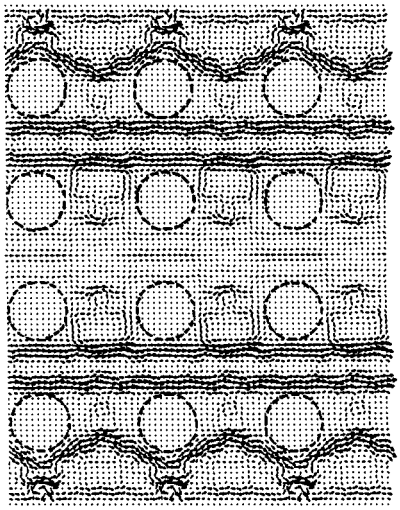

FIG. 5. The current density associated with state 8 in Fig. 2(a).

axis.) Analogously, the twofold degenerate states 5 and 6 correspond to electrons channeling between the upper and lower edges and the outer rows of antidots; see Fig. 4.

Before discussing the three remaining states, in which the current distribution is truly two-dimensional, let us investigate what happens to the five channeling states when a weak field is switched on. These states are all pseudo-one-dimensional in character. In a finite magnetic field, the degeneracy between channeling states is formally lifted, and each state will be located in a different channel between rows of antidots. However, from a physical point of view, the five different channeling states are essentially equivalent (the hard wall boundaries will perturb this simplest picture somewhat). With the Landau gauge used, the longitudinal wave number [dimension (length)$^{-1}$] $\mathscr{K}=K/a$ and the transverse coordinate y appear in the combination $\mathscr{K}-y/l_B^2$. Thus, the value of the parameter $\mathscr{K}$ simply fixes the transverse position of the pseudo-one-dimensional state in question. Two such states in neighboring channels are physically equivalent and should have the same dispersion relation, but shifted by $\Delta\mathscr{K}=\mathscr{L}/l_B^2$. This behavior is recognized in Fig. 2(b) where five free particle parabolas, appearing as essentially straight lines in the reduced zone representation, run parallel to one another. The shift is quantitatively accounted for by the formula $\Delta KL/\pi=\Delta\mathscr{K}\mathscr{L}/\pi=\pi^{-1}(\mathscr{L}/l_B)^2$ [the nondegeneracy between the twofold and threefold degenerate states in Fig. 2(a) explains the slight variation in the K shift].

Returning to the remaining states in zero magnetic field, Fig. 5 shows the current density profile associated with the state marked by the arrow 8 in Fig. 2(a). This state has appreciable dispersion, although its group velocity is somewhat lower than that of the channeling states 2–6. The current density still has a quasi-one-dimensional character but with some admixture of vortex formation.[39] In contrast to the states 2–6, where the wave functions have no nodes in the constrictions between antidots, the state under consideration has one or two nodes there.

Deviations from the one-dimensional character are much more pronounced for state 7 with a group velocity smaller than that of state 8. In this case the wave function has two nodes in most constrictions. The probability density is distributed equally in the horizontal and vertical channels between two neighboring rows of antidots and vortex flow is now a prominent feature. Generally, the more nodes the wave function has in the constrictions, the stronger the deviation from the one-dimensional character of the corresponding current.

In the case of the almost dispersionless state 1 of Fig. 2(a), the current completely loses its quasi-one-dimensional character; see Fig. 6. The probability to find an electron in some vertical channel is much higher than in a horizontal one. In the horizontal constrictions the wave function has typically three nodes.

To explain the origin of the different types of Bloch states and the characteristic features of the current density, let us consider electron transport in a single horizontal constriction defined by two neighboring antidots in the unit cell. The confinement by the antidot potential causes transverse quantization. With hard wall confinement, the energy of the electron in an eigenstate of the constriction is $E=(\hbar^2/2m^*)(k_\parallel^{j\,2}+k_\perp^{j\,2})$, where $k_\perp^j$ and $k_\parallel^j$ are the transverse and longitudinal wave numbers, and $k_\perp^j=\pi j/d$, with d the separa-

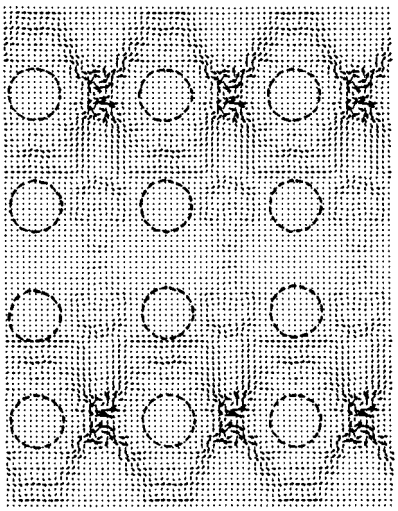

FIG. 6. The current density associated with state 1 in Fig. 2(a).

tion between antidots. With the parameters chosen here, only three transverse modes are propagating in the constriction. The lowest (ground) transverse state has even parity and no nodes. The next transverse states have odd parity and one node, etc. As shown by Szafer and Stone,[40] the state with the transverse wave number $k_\perp^j$ inside the constriction is mostly coupled to outgoing modes with transverse wave numbers close to $\pm k_\perp^j$ (with the spread given by the uncertainty relation[35]). From energy conservation this implies that longitudinal wave numbers of outgoing states are close to $k_\parallel^j$. Thus, at the exit of the constriction, the angular distribution of the electrons is roughly confined to a cone with an opening angle $\beta \sim \tan^{-1}[k_\perp^j/k_\parallel^j]$. In other words, it strongly depends on the subband index j inside the constriction. For the transverse ground state ($j=1$), $k_\perp^1 \ll k_\parallel^1$, and electrons are ejected from the constriction with a small opening angle β. The transverse states with one node ($j=2$) has a larger opening angle, and for the $j=3$ state, $k_\perp^3 \sim k_\parallel^3$, resulting in a wide angular distribution.

The qualitative nature of the Bloch states in the antidot lattice can be understood on the basis of the above analysis. The quasi-one-dimensional channeling states (2–6) are closely related to the transverse ground states in the constrictions, with their group velocity essentially determined by the longitudinal velocity $v=\hbar k_\parallel^1/m^*$ there. The narrow cone ejected from constriction ground states explains the quasi-one-dimensional character of these Bloch states. The slower states (7 and 8) correspond to mixtures of transverse constriction modes with one or two nodes. The associated wide opening angles β lead to a considerable probability for the electrons to be directed into the vertical channels between antidots, with a resulting vortex character of the flow in these Bloch states. Finally, the almost dispersionless state 1 has two or three nodes in the horizontal constrictions. This corresponds to the highest propagating ($j=3$) and lowest evanescent ($j=4$) mode there. Thus, one can view this Bloch state as one built from bound states in the space *between* antidots, weakly coupled through the constrictions by slowly propagating and evanescent modes.

C. Moderate magnetic fields

The magnetic field changes the band structure of an antidot array. Nevertheless, some of the features of the Bloch states, discussed above as characteristic for the case of zero magnetic field, can be recognized up to moderate fields, i.e., fields for which the cyclotron diameter $2r_c \gtrsim La$. The magnetic band structure of the antidot lattice at $B=0.255$ T is presented in Fig. 7 (this corresponds to the magnetic field when an electron classically encircles a group of four antidots at $n_s=1.5\times10^{15}$ m^{-2}; $2r_c=2La$). Fig. 8 shows the current density profile, associated with the state marked by arrow 1 in Fig. 7. This state combines features we have already discussed for the zero-field case. Through the channel marked A in Fig. 8, electrons propagate in a quasi-one-dimensional fashion, whereas in channel B laminar and vortex-type flow are equally prominent. A new type of flow pattern, absent in the case of zero magnetic field, is the one corresponding to rotation around an antidot (Fig. 8, upper row of antidots). We present the current density for one representative state only. Current densities associated with the

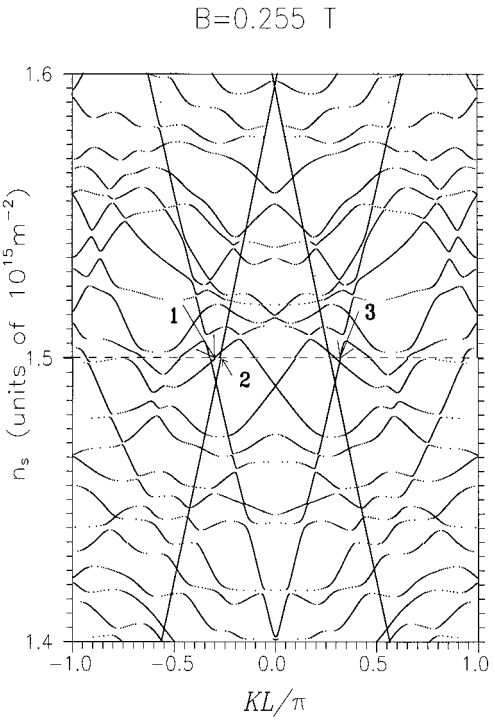

FIG. 7. Magnetic band structure of the antidot lattice at $B=0.255$ T. (The classical cyclotron orbit encircles a group of four antidots, $2r_c=2La$ at $n_s=1.5\times10^{15}$ m^{-2}.)

rest of the states (except those marked by arrows 2 and 3) exhibit very similar features in the sense that in each state one can recognize quasi-one-dimensional flow, regions where laminar and vortex aspects compete, and flow circulating around an antidot (or in the space between antidots).

The quasi-one-dimensional electron states (2 and 3) are nothing but the familiar edge states located close to the upper edge (right moving state) or lower edge (left moving state) of the structure; see Fig. 9. These edge states are essentially identical to those of a perfectly homogeneous strip (without the antidot potential). The transverse extent of an edge state is of the order of the magnetic length, $l_B=(\hbar/eB)^{1/2}$. When

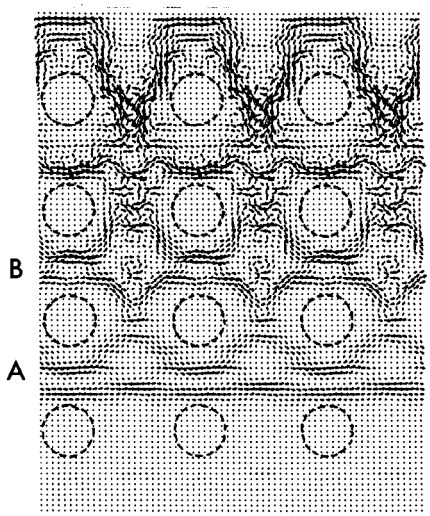

FIG. 8. The current density associated with state 1 in Fig. 7.

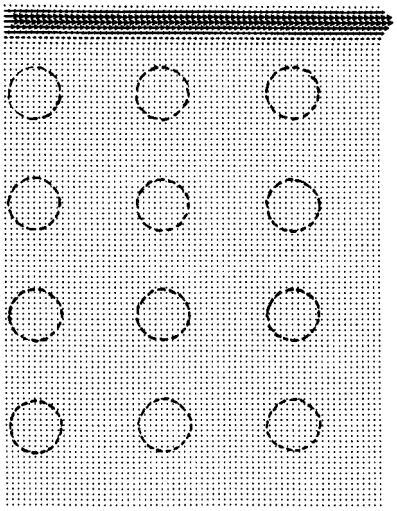

FIG. 9. The current density associated with state 2 in Fig. 7.

l_B is smaller than the distance between the boundary and the nearest antidot row, the edge state does not ''feel'' the presence of the antidots and, consequently, its dispersion is the same with and without antidots. Conversely, with larger l_B or with several edge states increasingly removed from the boundary, some of the edge states existing in the homogeneous channel are blocked here by the presence of antidots. Thus, the number of edge states in the antidot structure equals the number of those edge states in the corresponding homogeneous channel for which the transverse localization length is less than the distance between the boundary and the closest antidots. With an increasing magnetic field, the magnetic length l_B decreases. Therefore, more edge states can be accommodated in the space between the upper edge and the upper row of antidots. The state closest to the upper edge is the one with the lowest transverse energy, i.e., with the highest group velocity. Of the two edge states represented in Fig. 7 the one with the highest slope is clearly 2. Note that the linearity of the dispersion curves for the edge states is only apparent. The ''lines'' are small segments of essentially parabolic dispersion curves.

D. Magnetic field of the single-antidot resonance

Figure 10 shows the band structure of the antidot lattice at $B=0.51$ T, which corresponds to the case when the classical cyclotron diameter equals the period of the antidot lattice ($2r_c=La$ at $n_s=1.5\times10^{15}$ m^{-2}). This is the parameter range in which pronounced features have been observed in the linear response of devices with an antidot lattice. These features have often been attributed to electron orbits encircling single antidots. From Fig. 10 it is clear that the energy corresponding to precisely $n_s=1.5\times10^{15}\,\mathrm{m}^{-2}$ is not a good choice, since the number of Bloch states is exceptionally low here. We choose, instead, to investigate the magnetic Bloch states at $n_s=1.525\times10^{15}$ m^{-2}. The states marked by 1 and 2 are the edge states, with state 1 closer to the edge. The state 3 is a quasiedge state. It is located, like ordinary edge states, close to the upper edge of the structure, but its transverse extent is sufficiently large that the current distribution is somewhat perturbed by the uppermost row of antidots, with an admixture of vortex character. Surprisingly, only one state

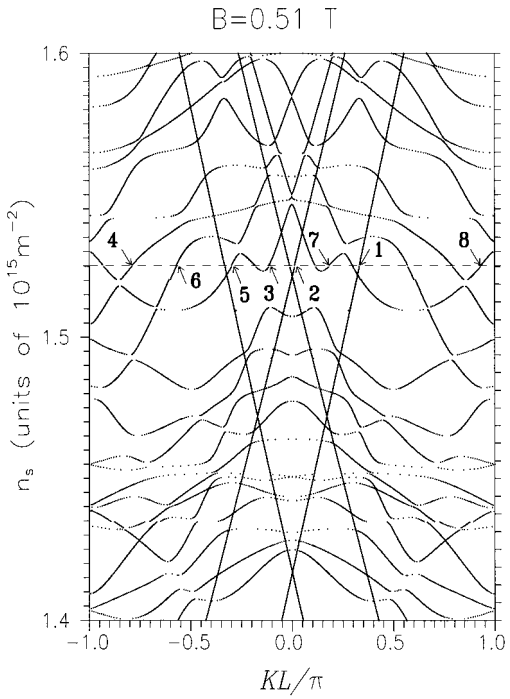

FIG. 10. Magnetic band structure of the antidot lattice at $B=0.51$ T. (The classical cyclotron orbit encircles a single antidot, $2r_c=La$ at $n_s=1.5\times10^{15}$ m^{-2}.)

(4) from the remaining set (4–8) is characterized by a rotational flow around a single antidot; see Fig. 11. The current density patterns associated with the states 5–8 are, on the other hand, strikingly reminiscent of the classical ''runaway'' trajectories[16] found in this parameter range, where electrons channel between two rows of antidots by bouncing off successive antidots down the channel; see Fig. 12. Here we show the particle density flow for one selected state (5) only. The remaining states (6–8) have the same character, but are localized in different horizontal channels.

E. High magnetic fields

When the magnetic field is increased beyond the value that corresponds to the classical commensurabilty ''reso-

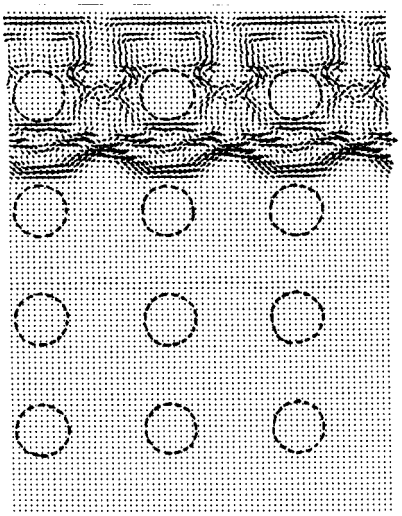

FIG. 11. The current density associated with state 4 in Fig. 10.

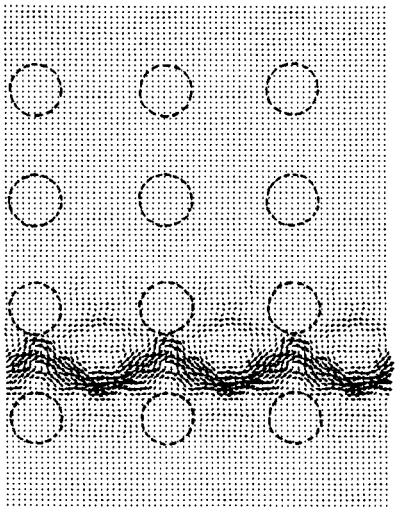

FIG. 12. The current density associated with state 5 in Fig. 10.

nance,'' $2r_c = La$, the band structure undergoes significant changes. Classically, with a cyclotron diameter smaller than the superlattice period, one would expect an increasing fraction of the electrons to get trapped around single antidots or in the space between antidots. When $2r_c < d$, with d the distance between antidots, *all* classical trajectories are completely localized, and transport is possible by means of skipping orbits at the edges of the structure only. These classical facts are reflected in the quantum-mechanical band structure, which shows a drastic reduction of the number of propagating Bloch states in magnetic fields $B > B_c$, where B_c is the magnetic field corresponding to the single antidot resonance, $2r_c = La$; see Fig. 13. Note that the majority of Bloch states at $B > B_c$ are edge states.

Figure 14(a) shows the dispersion relations at $B = 0.765$ T [$2r_c = (2/3)La$ at $n_s = 1.5 \times 10^{15}$ m^{-2}]. For comparison, we present the band structure for a corresponding homogeneous channel (without the antidot potential) in Fig. 14(b). Most edge states in the homogeneous strip have their counterparts with an antidot lattice, only one of them is blocked by the outer rows of antidots.

The remaining states in the antidot lattice are slow ones with small dispersion (except the state 2, the origin of which we shall discuss below). The current density of state 1, representative in this context, is shown in Fig. 15. The current corresponds to some extent to counterclockwise electron rotation around single antidots, but mostly to such motion in the space between antidots. This indicates that the origin of these minibands is quasi-bound states in the antidot array. In this field region, transport through the antidot lattice resembles that of the extreme quantum regime considered in Ref. 28, where all minibands (except the edge states) were associated with electrons trapped around single antidots or in the space between antidots.

Finally, let us consider state 2, which has an appreciable dispersion and a current density, Fig. 16, distinct from those of the miniband states discussed so far. The origin of this state can be understood as follows. In the homogeneous strip, four magnetic edge states are allowed; see Fig. 14(b). With antidots present, one of them is blocked by the first row of antidots. The total width of the system is sufficiently large that direct backscattering to the opposite edge is completely

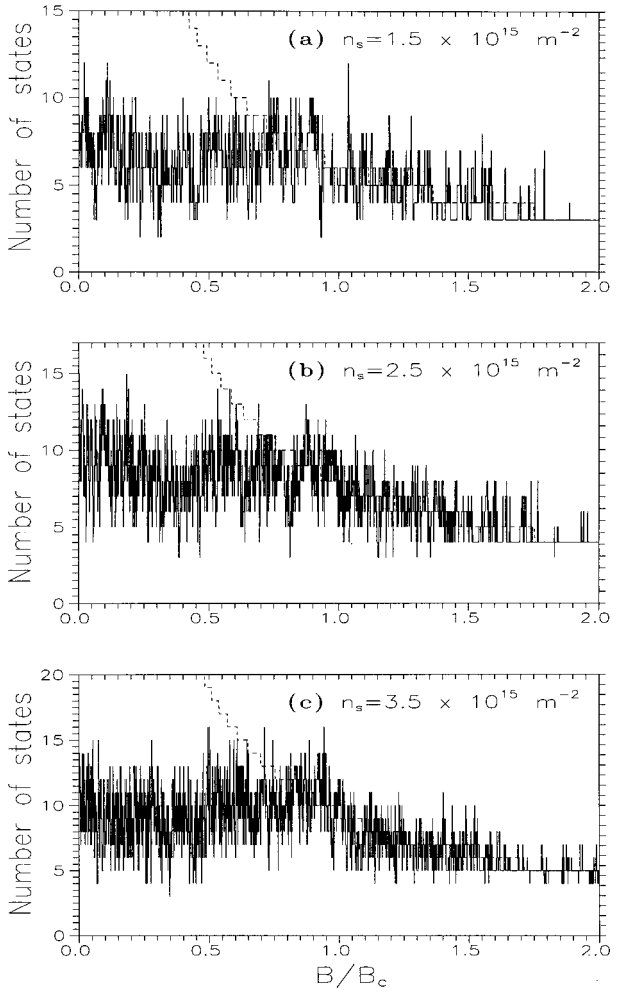

FIG. 13. The dependence on the magnetic field of the number of propagating Bloch states in the antidot lattice for different sheet electron densities (solid lines). The dashed lines represent the number of propagating states in the corresponding homogeneous strip. B_c is the magnetic field corresponding to the single antidot resonance, $2r_c = La$.

negligible. Scattering across the entire system is only possible via bulk states in the structure. If, at the given energy and magnetic field, such states are absent, reflection is completely suppressed and the fourth ''edge'' state is forced to strike a compromise between edge localization and transport through the antidot array. The nature of this compromise is displayed in Fig. 16. The deviation from strictly one-dimensional motion is highlighted by the vortices between the edge and the first row of antidots. On the other hand, the basically one-dimensional character of this state is emphasized by the small band gap at the reduced zone boundaries $KL/\pi = \pm 1$ at $n_s \approx 1.46 \times 10^{15}$ m^{-2}.

For still higher magnetic fields when, for example, $2r_c = (1/2)La$, transport in the antidot lattice is essentially only possible by edge-state propagation; see Fig. 17. In this case the localization length $\sim l_B = 25$ nm is much smaller than the distance between neighboring antidots. Thus, the coupling between bound states around or between antidots is greatly suppressed. This is reflected in the appearance of a few very narrow minibands with almost zero dispersion. It is

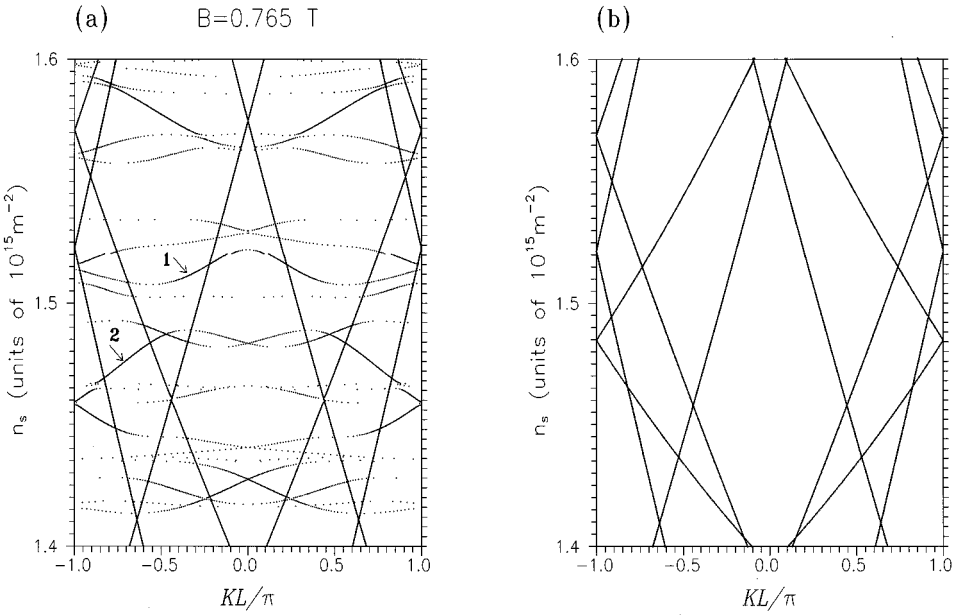

FIG. 14. (a) Magnetic band structure of the antidot lattice at $B=0.765$ T $[2r_c=(2/3)La$ at $n_s=1.5\times10^{15}$ m$^{-2}]$. (b) Dispersion relations for corresponding homogeneous strip.

only in these narrow bands that the antidot array makes its presence felt. As a result, one should expect that, in this parameter region, the transport properties of antidot arrays are almost indistinguishable from those of a perfect strip.

At this point it is natural to comment on similarities and differences with respect to our previous work. In Ref. 28 we studied transport in the extreme quantum regime, with one or two Landau levels only, and with the Fermi wavelength of the same order as the superlattice constant. In that regime the complexities at low magnetic field, reminiscent of those arising from a description in terms of classical chaotic trajectories, are absent. On the other hand, at high fields the similarities with our present results are striking. In both cases edge transport dominates, with intermittent energy bands representing bulk hopping between quasilocalized states. The width of these bands is determined by the overlap of the correponding states. In the present case, this overlap is considerably smaller than in Ref. 28, simply because the ratio l_B/La is smaller.

F. Bloch states versus classical trajectories

A number of discussions of transport in antidot arrays are based on an analysis of classical electron trajectories. This strategy has been quite successful in describing the gross features of transport through large arrays. Our approach is similar in the sense that we can discuss detailed spatial aspects of the transport process. However, our starting point is radically different in that we consider typical Bloch states for coherent transport. Leaving aside the considerable complications added by the existence of a finite coherence length, the connection between Bloch states and classical trajectories is, in principle, clear: Classical electron trajectories are limiting forms of moving wave packets that are judiciously chosen linear combinations of Bloch states. In practice, one is far from having a full understanding of the relations between the two descriptions. In this context we restrict ourselves to a few simple remarks.

For very low fields we find that transport is dominated by a set of ''channeling'' Bloch states, with current density con-

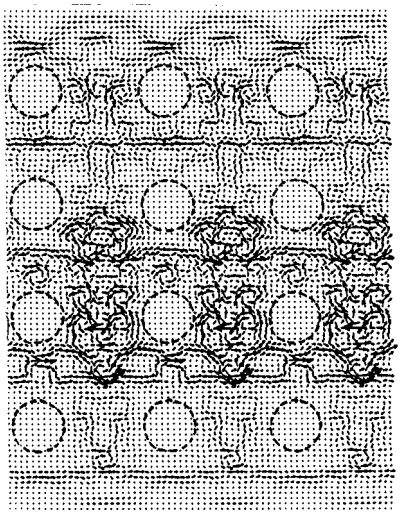

FIG. 15. The current density associated with state 1 in Fig. 14(a).

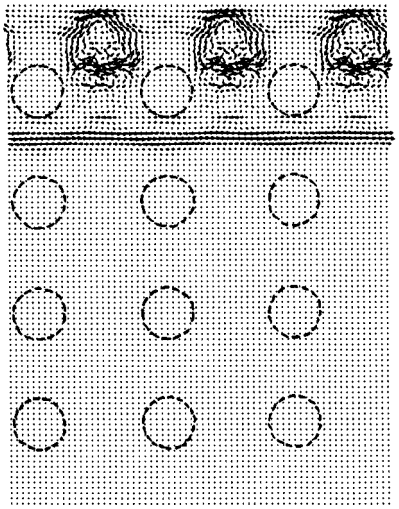

FIG. 16. The current density associated with state 2 in Fig. 14(a).

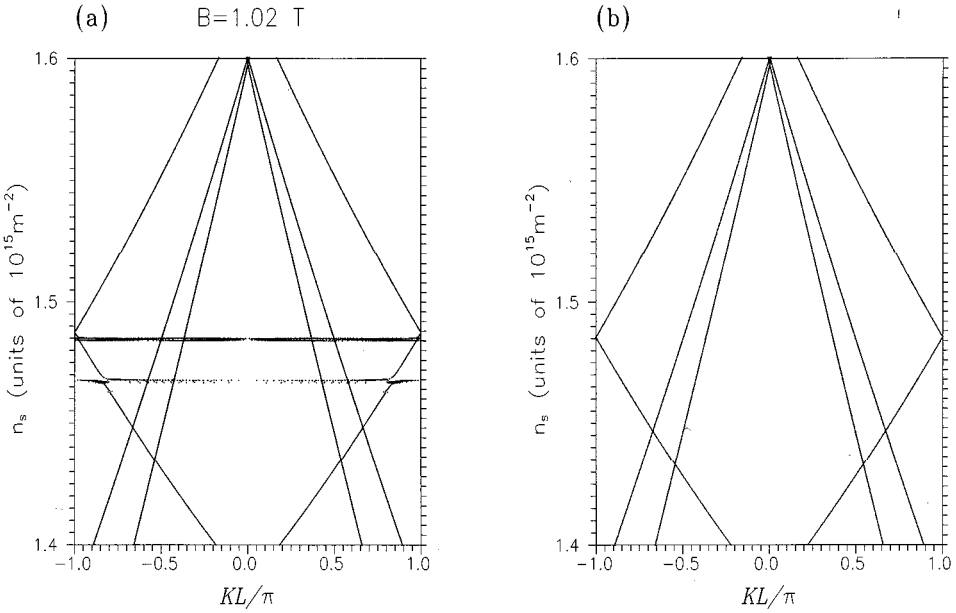

FIG. 17. (a) Magnetic band structure of the antidot lattice at $B=1.02$ T $[2r_c=(1/2)La$ at $n_s=1.5\times10^{15}$ m$^{-2}]$. (b) Dispersion relations for corresponding homogeneous strip.

centrated in the channels between rows of antidots. Very similar trajectories are found to dominate in the classical regime.[14,20] In the field range where the cyclotron diameter matches the period of the antidot lattice, we do find Bloch states that display rotational flow around single antidots. (Note that states that describe *completely* localized electrons cannot exist as Bloch states.) But the most striking feature in this field range is the existence of channeling Bloch states of the runaway type, reflected periodically from antidots on one side of the channel. This is consistent with the findings on classical arrays by Baskin *et al.*,[16] who stress the dominance of runaway trajectories over pinned orbits. However, the pinning effect in antidot lattices is manifested indirectly, by the drastic reduction of the number of propagating Bloch states in magnetic fields $B>B_c$.

Note that the detailed properties of the antidots are expected to be quite important for these effects, in both the quantum and the classical case. We are not yet in a position to discuss the influence of such details with confidence. More work needs to be done on these aspects.

Finally, quantum edge states have, as is well known, their counterpart in classical skipping orbits.

IV. SUMMARY

On the basis of an efficient hybrid numerical technique we have, in this paper, studied the band structure of a regular array of antidots, confined in the y direction and infinite in the x direction. In particular, we have investigated how this band structure changes as the applied magnetic field is increased, and how the character, as represented by their current densities, of the corresponding Bloch states evolves. In a sequel to this paper we shall use the results obtained here in a discussion of the two-terminal conductance of finite antidot arrays.

ACKNOWLEDGMENTS

The authors have benefited from most valuable discussions with K.-F. Berggren, K. Ensslin, J. P. Kotthaus, D. Weiss, and H. Xu. I.V.Z. is indebted to NTH and Norges Forskningsråd for financial support.

*Present address: Department of Physics and Measurement Technology, Linköping University, S-581 83 Linköping, Sweden.

[1] K. Ensslin and P. M. Petroff, Phys. Rev. B **41**, 12 307 (1990).
[2] C. G. Smith, M. Pepper, R. Newbury, H. Ahmed, D. G. Hasko, D. C. Peacock, J. E. F. Frost, D. A. Ritchie, G. A. C. Jones, and G. Hill, J. Phys. Condens. Matter **2**, 3405 (1990).
[3] A. Lorke, J. P. Kotthaus, and K. Ploog, Phys. Rev. B **44**, 3447 (1991).
[4] D. Weiss, P. Grambow, K. von Klitzing, A. Menschig, and G. Weimann, Appl. Phys. Lett. **58**, 2960 (1991).
[5] D. Weiss, M. L. Roukes, A. Menschig, P. Grambow, K. von Klitzing, and G. Weimann, Phys. Rev. Lett. **66**, 2790 (1991).
[6] G. M. Gusev, Z. D. Kvon, L. V. Litvin, Yu. V. Nastaushev, A. K. Kalagin, and A. I. Toropov, J. Phys. Condens. Matter. **4**, L269 (1992); G. M. Gusev, Z. D. Kvon, L. V. Litvin, Yu. V. Nastaushev, A. K. Kalagin, and A. I. Toropov, Superlatt. Microstruct. **13**, 383 (1993); **13**, 263 (1993).
[7] G. Berthold, J. Smoliner, V. Rosskopf, E. Gornik, G. Böhm, and G. Weimann, Phys. Rev. B **45**, 11 350 (1992); **47**, 10 383 (1993).
[8] R. Schuster, K. Ensslin, J. P. Kotthaus, M. Holland, and C. Stanley, Phys. Rev. B **47**, 6843 (1993).
[9] D. Weiss, K. Richter, A. Menschig, R. Bergmann, H. Schweizer, K. von Klitzing, and G. Weimann, Phys. Rev. Lett. **70**, 4118 (1993).
[10] F. Nihey and K. Nakamyra, Physica B **184**, 398 (1993).
[11] R. Schuster, K. Ensslin, D. Wharam, S. Kühn, J. P. Kotthaus, G. Böhm, W. Klein, G. Tränkle, and G. Weimann, Phys. Rev. B **49**, 8510 (1994).
[12] R. Schuster, G. Ernst, K. Ensslin, M. Entin, M. Holland, G. Böhm, and W. Klein, Phys. Rev. B **50**, 8090 (1994).
[13] T. Deruelle, B. Meurer, Y. Guldner, J. P. Vieren, M. Riek, D. Weiss, K. von Klitzing, K. Eberl, and K. Ploog, Phys. Rev. B **49**, 16 561 (1994).
[14] F. Nihey, S. W. Hwang, and K. Nakamyra, Phys. Rev. B **51**, 4649 (1995).

[15] R. Fleischmann, T. Geisel, and R. Ketzmerick, Phys. Rev. Lett. **68**, 1367 (1992).
[16] E. M. Baskin, G. M. Gusev, Z. D. Kvon, A. G. Pogosov, and M. V. Entin, Pis'ma Zh. Éksp. Teor. Fix. **55**, 649 (1992) [JETP Lett. **55**, 678 (1992)].
[17] H. Silberbauer, J. Phys. Condens. Matter **4**, 7355 (1992).
[18] D. Huang and G. Gumbs, Phys. Rev. B **48**, 2835 (1993); D. Huang, G. Gumbs, and A. H. MacDonald, *ibid*. **48**, 2835 (1993).
[19] R. B. S. Oakeshott and A. MacKinnon, J. Phys. Condens. Matter **6**, 1519 (1994).
[20] R. Fleischmann, T. Geisel, R. Ketzmerick, and G. Petschel, Semicond. Sci. Technol. **9**, 1902 (1994).
[21] H. Silberbauer and U. Rössler, Phys. Rev. B **50**, 11 911 (1994).
[22] S. Ishizaka, N. Nihey, K. Nakamura, J. Sone, and T. Ando, Phys. Rev. B **51**, 9881 (1995).
[23] D. Hofstadter, Phys. Rev. B **14**, 2239 (1976).
[24] C. W. J. Beenakker and H. van Houten, in *Solid State Physics, Advances in Research and Applications*, edited by H. Ehrenreich and D. Turnbull (Academic, San Diego, 1991), Vol. 44.
[25] R. Landauer, Phys. Lett. **85A**, 91 (1981); D. S. Fisher and P. A. Lee, Phys. Rev. B **23**, 6851 (1981); M. Büttiker, Phys. Rev. Lett. **57**, 1761 (1986); R. Landauer, J. Phys. Condens. Matter **1**, 8099 (1989); A. D. Stone and A. Szafer, IBM J. Res. Dev. **32**, 384 (1988).
[26] D. S. Fisher and P. A. Lee, Phys. Rev. B **23**, 6851 (1981).
[27] R. B. Laughlin, Phys. Rev. B **23**, 5632 (1981); B. I. Halperin, *ibid.* **25**, 2185 (1982); A. H. MacDonald and P. Streda, *ibid.* **29**, 1616 (1984).
[28] I. V. Zozulenko, F. A. Maaø, and E. H. Hauge, Phys. Rev. B **51**, 7058 (1995).
[29] I. V. Zozoulenko, F. A. Maaø, and E. H. Hauge, following paper, Phys. Rev. B **53**, 7987 (1996).
[30] E. Brown, Phys. Rev. **133**, A1038 (1964); J. Zak, *ibid.* **134**, A1607 (1964).
[31] See, e.g., H. Xu, Z. L. Ji, and K.-F. Berggren, Superlatt. Microstruct. **12**, 237 (1992).
[32] H. Xu, Phys. Rev. B **50**, 8469 (1994); **12**, 254 (1994).
[33] A. MacKinnon, Z. Phys. B **59**, 385 (1985).
[34] F. Sols, M. Macucci, U. Ravaioli, and K. Hess, J. Appl. Phys. **66**, 3892 (1989).
[35] F. A. Maaø, I. V. Zozulenko, and E. H. Hauge, Phys. Rev. B **50**, 17 320 (1994).
[36] L. D. Landau and E. M. Lifshitz, *Quantum Mechanics* (Pergamon Press, Oxford, 1965).
[37] M. Leng and C. S. Lent, Phys. Rev. B **50**, 10 823 (1994).
[38] J. Skjånes, G. Schön, and E. H. Hauge, Phys. Rev. B **50**, 8636 (1994).
[39] The formation of laminar and vortex patterns in electron flow in nanostructures was discussed in K.-F. Berggren, C. Besev, and Zhen-Li Ji, Phys. Scr. **T42**, 141 (1992).
[40] A. Szafer and A. D. Stone, Phys. Rev. Lett. **62**, 300 (1989).